# Multi-scale analysis of textural atomization in LOx-CH4 rocket engine subcritical flames

Leonardo Geiger, Nicolas Fdida, Luc-Henry Dorey, Lucien Vingert, Marie Théron, Christophe Dumouchel, Jean-Bernard Blaisot

# MULTI-SCALE ANALYSIS OF TEXTURAL ATOMIZATION IN $LO_X$-$CH_4$ ROCKET ENGINE SUBCRITIAL FLAMES

**SPACE PROPULSION 2024**
GLASGOW, SCOTLAND | 20 – 23 MAY 2024

**Leonardo Geiger [1,2,3], Nicolas Fdida [1], Luc-Henry Dorey [1], Lucien Vingert [1], Marie Théron [3], Jean-Bernard Blaisot [2], Christophe Dumouchel [2]**

*[1] DMPE, ONERA, Université Paris Saclay, F-91123 Palaiseau, France, Email : Leonardo.Geiger@onera.fr*
*[2] CORIA, CNRS, Normandie Université UNIROUEN, INSA ROUEN, Rouen, France*
*[3] CNES, Space Transportation, Paris, France*

**KEYWORDS:** Cryogenic propulsion, atomization, droplet size distribution, multi-scale analysis.

**ABSTRACT:**

In cryogenic liquid rocket engines, the propellants are usually injected into the combustion chamber by a coaxial injection system. During transient or low-thrust flight regimes, the injected propellants are in a subcritical state. The oxidizer is injected as a cylindrical liquid jet and the fuel is injected as a higher-velocity annular gaseous stream surrounding the liquid. Under such conditions, the primary atomization of the liquid oxidizer plays a major role in the combustion process. The primary atomization of the liquid oxidizer refers to the production of liquid fragments and droplets from ligaments at the liquid-gas interface. These ligaments, most likely a result of turbulent fluctuations in the liquid jet, are peeled from the interface in a process referred to as textural atomization. This article proposes a multi-scale description of the liquid ligaments responsible for the primary atomization process in a liquid oxygen/methane powered subscale rocket combustor. This description relies on recently developed image processing techniques to measure the local scale distribution of the liquid ligaments, as visualized in experimental backlighting images of the atomization process. Results report an evolution of the scale distribution of textural ligaments with the distance from the injector. Three operating conditions are compared. A global trend is observed, including positions where the textural atomization process is at its most intense and where it stops. A weak dependency on chamber pressure is reported, which is in line with the turbulent fluctuation-based ligament initiation scenario proposed in the literature. The reported measurements may lead to an estimation of local drop-diameter distributions. The reported observations provide valuable insights into the primary atomization process which can be used in the development of numerical models.

## 1. INTRODUCTION

The development of throttleable and relightable liquid rocket engines (LRE), necessary to equip future launchers, requires the use of detailed numerical models that can reproduce the physical processes involved in engine operation. One of these processes is the primary atomization during combustion of the cryogenic propellants. During transient or low-thrust engine operating phases, primary atomization is a major contributor to the efficiency and stability of the combustion process. The propellants are injected into the combustion chamber in a subcritical state, i.e. their pressure or temperature are below their critical point values [1]. In the case of coaxial assisted atomization, a round liquid jet of oxidizer is injected surrounded by a high-velocity annular flow of gaseous fuel [2]. The injection conditions usually found in LREs lead to a fiber-type atomization regime, according to the classification proposed by Lasheras and Hopfinger [3]. This regime is characterized by the peeling of the interface leading to the formation of small, fiber-like liquid structures. The process responsible for the peeling of these fiber-like structures is known as textural atomization [4] since their size is much smaller than that of the liquid bulk. These textural structures, ligamentous in shape, are at the origin of the production of droplets in the vicinity of the liquid jet.

Previous studies on the primary breakup of liquid jets have proposed that the appearance of ligaments issuing from the liquid bulk is the result of turbulent eddies in the liquid phase overcoming the surface tension effects at the liquid-gas interface [5,6]. Other studies associate the production of ligaments as a result from the development of surface instabilities at the interface [7,8]. In all cases, a spatial evolution in ligament number and size is observed.

Primary atomization occurs in the vicinity of the liquid jet, a zone where propellants evaporate, mix and react, resulting in strong density, temperature and composition gradients. These conditions result in strong optical index gradients, which pose challenges for the measurement of the spray characteristics.

This work proposes a description of the primary atomization process through the measurement of scale distributions [4] of the liquid ligaments visualized experimentally in the near-injector region of a subscale liquid oxygen (LOx)-methane ($CH_4$) rocket combustor. Three subcritical operating conditions are considered to study and compare the textural atomization process.
The following section describes the experimental set-up and the optical apparatus used for the visualization of the liquid oxygen jet and ligaments. Next is a section describing the multi-scale measurement methodology, followed by a section detailing the image processing. Finally, the main results are presented, followed by a conclusion.

## 2. EXPERIMENTAL WORK

The experimental work was performed in ONERA's MASCOTTE test-bench [10]. This subscale cryogenic rocket combustor is capable of reproducing operating conditions similar to those encountered inside the combustion chambers of LREs. It is designed to allow the study of fundamental physical processes occurring inside the combustion chamber of such engines using imaging diagnostics [11]. These include, among others, the injection, atomization and combustion of the propellants, the onset of combustion instabilities [12], as well as heat transfer [13] and soot formation in LOx/$CH_4$ jet flames [14]. The combustion chamber used during tests is water-cooled and designed to operate at conditions representative of real rocket engine main chambers, i.e. high pressures and high mixture ratios.
The injection system is composed of a single shear-coaxial injector with no recess between the liquid and the gas injector-tube exit planes. The system injects a liquid jet of oxidizer (liquid oxygen) through a central circular tube surrounded by a high-speed gaseous fuel (methane) flow injected from an annular tube.
The LOx/$CH_4$ propellants are injected in a subcritical state, i.e. their pressure and temperature are below their critical point values [1]. Three operating points are tested, with varying chamber pressures $P_c$. The mixing ratio $M$ is close to its stoichiometric value ($M_{st} = 4$) and is kept nearly constant for all tests, and the liquid Reynolds number $Re_L$, based on the Lox injector diameter, is kept as constant as possible given the experimental constraints. Consequently, the momentum flux ratio $J$ and the gas density $\rho_G$ vary across the different operating points. Table 1 summarizes the main parameters defining the achieved operating points. According to the assisted atomization regime classification from Lasheras and Hopfinger [3], the tested operating conditions place the atomization process in a fiber-type breakup regime.

*Table 1. Tested operating conditions*

| O.C. | $p_c$ (bar) | $J$ | $M$ | $Re_L$ | $We_R$ | $\rho_L/\rho_G$ |
|---|---|---|---|---|---|---|
| A | 7 | 15 | 3.5 | $7.7 \times 10^4$ | $4.6 \times 10^4$ | 224 |
| B | 10 | 10 | 3.5 | $9.1 \times 10^4$ | $4.4 \times 10^4$ | 150 |
| C | 15 | 8 | 3.2 | $1.2 \times 10^5$ | $5.9 \times 10^4$ | 97 |

The experiments are performed under LOx/$CH_4$ combustion conditions. The propellants are ignited by a hydrogen-oxygen torch igniter. Under combustion, a spray of very fine droplets produced in the near-field region (near the injector) is rapidly evaporated and burned with the fuel. This fast consumption of the spray allows the visualization of the liquid jet core shown in Fig. 1. In addition to the liquid phase, Fig. 1 also shows that the visualization of the near-field zone around the liquid jet is affected by optical index gradients caused by the strong temperature and density gradients in the flow. The presence of these strong index gradients, in addition to severe conditions including flame luminosity and particle depositions on the windows, makes the investigation of the spray in the near-field very difficult. In the present work, an imaging method is used to visualize the liquid jet core in the vicinity of the injector exit.
The combustion chamber is equipped with two opposite rectangular quartz optical windows of 25 mm x 60 mm, used to record images of the flow by adopting a backlighting optical arrangement. It includes a laser source (Cavilux Smart 400 W laser emitting a red incoherent light pulse of 1-1.5 µs duration and at a wavelength of 640 ± 10 nm) and a camera (JAI GOX-2402, 1920 x 1200 pixels with a pixel size = 3.45 µm) recording 50 images per second. The visualization of small-scale interfacial liquid structures and their measurement using a multiscale approach requires the highest possible spatial resolution. Therefore, the camera is equipped with a long-distance microscope Infinity K2 DistaMax with a CF1/B lens. This setup results in a field of view of 8.64 mm x 5.40 mm, with a spatial resolution of 4.5 µm/pixel, as presented in Fig. 2. Additionally, a narrow band filter is used to block the light from the flame emission and to select only the light emitted by the laser source.
To investigate the spatial evolution of the textural atomization process, images were recorded at four positions with increasing distance from the injector.

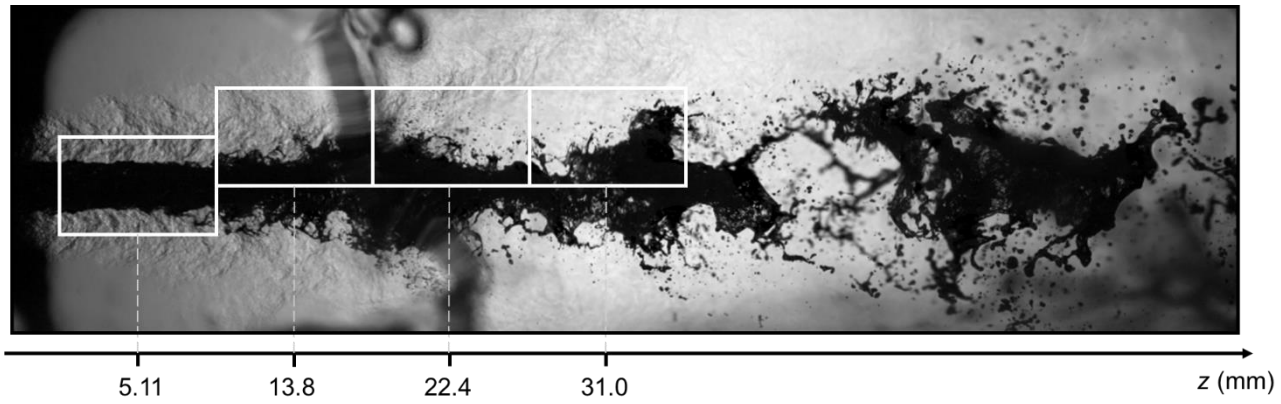


*Figure 1. Visualization of the entire optical window showing the atomization process under liquid oxygen/methane combustion for O.C. A in the MASCOTTE test-bench. White rectangles indicate the corresponding positions of the four series of high-resolution images used in this study.*

These images, whose positions are shown in Fig. 1 as white rectangles, are centered at $z$ = 5.11 mm, 13.8 mm, 22.4 and 31.0 mm, where $z$ is the distance from the injector plane. The position farthest from the injector ($z$ = 31.0 mm) is only used for images of operating point B. Images centered at $z$ = 13.8 mm, $z$ = 22.4 mm and $z$ = 31.0 mm show only the upper interface of the liquid jet (see Fig. 2), whereas images centered at $z$ = 5.11 mm show both the upper and bottom interfaces. Fig. 2 shows an instantaneous image from the high-resolution backlighting visualization of O.C. A at position $z$ = 22.4 mm. At each position, 100 images were recorded during the stationary phase of the reactive flow.

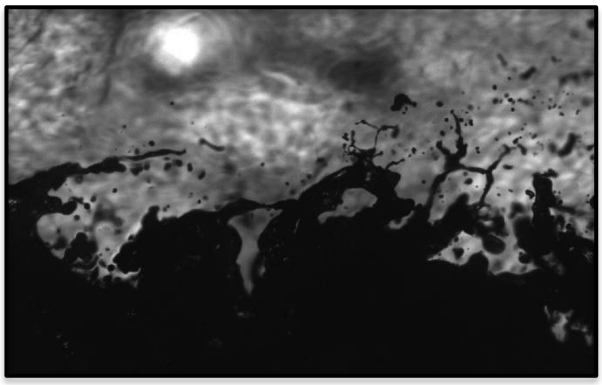

*Figure 2. Instantaneous high-resolution backlighting image (O.C. A, z = 22.4 mm).*

## 3. MULTI-SCALE DESCRIPTION

The description of the textural atomization process proposed here relies on the multi-scale analysis introduced in previous works [4, 15, 16]. This description consists in analysing a liquid system (such as the one visualized in the backlighting images of the primary atomization process introduced previously) as well as all systems parallel to it inside the liquid phase. These parallel systems are those obtained by erosion operations on the original liquid system. An erosion operation consists of removing, at the liquid-gas interface, a layer of liquid by dragging a disk of diameter $d$ along its interface while keeping the center of the disk on the interface line. The liquid system that remains after this operation is called the system eroded at scale $d$. Performing this operation for all possible values of $d$ ranging from 0 to the maximum scale of the liquid system (smallest scale for which erosion erases all the liquid system) allows to obtain all parallel systems. These systems are described by their surface area $S(d)$, their interface length $L(d)$, and their length-integrated curvature $H(d)$ [16].

The description of the visualized liquid system is based on the measurement of $S(d)$ from the experimental images. The details of the corresponding image processing are described in the next section. The function $S(d)$ is used to determine the cumulative scale distribution $E_2(d)$, defined as $E_2(d) = S(0) - S(d)$. The derivative of $E_2(d)$ with respect to the scale $d$ is the scale distribution $e_2(d)$, which is proportional to the interface length: $e_2(d) = L(d)/2$ [16]. The derivative of the scale distribution with respect to the scale, $e_2(d)_{,d}$, is used. It has been shown [4] that $e_2(d)_{,d}$ relates to the diameter distribution $f_{0c}(D)$ of the ensemble of $N_c$ cylinders of equal length $L_c$ that has the same scale distribution, as:

$$-e_2(d)_{,d} = N_c L_c f_{0c}(D)|_{D=d} \qquad (1)$$

If $f_{0c}(D)$ is mono-modal, Eq. 1 implies that $e_2(d)_{,d}$ reports one peak. In addition, since $f_{0c}(0) = 0$, $-e_2(0)_{,d} = 0$. When applied to experimental images of the interface, whose texture is made of ligamentous structures showing a series of contracted or swollen sections, $e_2(d)_{,d}$ characterizes the distribution of these sections.

## 4. IMAGE PROCESSING

The experimental images undergo a series of processing steps before being analysed with the multi-scale approach described in the previous section. Images are normalised to reduce local lighting inhomogeneities. This is achieved by the division of the images by an image of the

background without the presence of the flow. The normalised images are segmented to separate the liquid phase from the gas. This is performed using the ImageJ local Phansalkar thresholding algorithm [17] with a square local analysing window of 135 µm side length. The resulting images show the liquid phase in black against a white background. In addition, all liquid structures detached from the liquid core are eliminated, and eventual white holes inside the liquid phase are filled with back pixels.

The surface areas $S(d)$ of the liquid system and its parallel systems are measured on the segmented images by applying an Euclidean Distance Map (EDM) operation on the images. This operation attributes, to each liquid pixel, a brightness level equal to the shortest distance between the pixel and the interface. The surface area $S(d)$ corresponds to the number of pixels with a brightness level equal or larger than $d/2$. Then, once the surface areas $S(d)$ have been measured, the cumulative scale distribution $E_2(d)$ and its successive derivatives $e_2(d)$ and $e_2(d)_{,d}$ can be determined, as introduced in the previous section. The derivation is performed using a central finite difference scheme, and each derivation is preceded by a 3-point moving-average smoothing of the function.

The application of the measuring method, as described above, on individual synthetic images (simple objects whose theoretical solutions are known) shows a relative agreement between the measurements and the theoretical solutions. Fig. 3 considers an example of synthetic image showing a cylinder deformed by a sinusoidal perturbation of wavelength equal to 800 pixels and amplitude equal to 31 pixels. The unperturbed cylinder diameter is 70 pixels. The theoretical expression for $-e_2(d)_{,d}$ has been introduced and discussed in previous works [8,16] and is plotted in Fig. 4. The solution shows two discontinuities at scales $d_1$ = 8 pixels and $d_2$ = 132 pixels, which correspond to the diameter of the cylinder at the contracted and swelling sections respectively.

The resulting $-e_2(d)_{,d}$ distribution agrees with the overall shape of the theoretical solution. However we can notice small differences, mainly due to the pixelization of the image (a smooth object being described by a set of square pixels). These measurement errors have been tackled by using two additional steps in the measurement. These two steps have been introduced previously [8].

The first step is a sub-pixel treatment of the raw images through a $NxN$ bilinear interpolation on the pixel grey-levels. $N$ corresponds to the factor by which each pixel side length is divided, leading to a spatial resolution multiplied by $N$. This step leads to a more precise capture of the peaks in $-e_2(d)_{,d}$ describing the discontinuities.

The second additional step is a modification on the measurement of $S(d)$, allowing the surface areas to be equal to non-integer numbers of pixels, leading to a more accurate measurement of S(d) and reducing the oscillations in the resulting distribution.

Fig. 4 reports the $-e_2(d)_{,d}$ distribution measured using these two additional steps and compares it to the theoretical solution. The use of these additional steps removes almost all disagreements between the measurement and the theoretical solution. The only remaining disagreement is at vary small scales ($d$ < 5 pixels), as seen by a peak at d = 0. This is a persisting effect of the image pixelization. This effect, however, is dissociated from the scales of interest when the sub-pixel factor $N$ is sufficiently high. This result shows that the image processing described can be used to measure the scale distribution $e_2(d)$ and its derivative $e_2(d)_{,d}$ of a deformed object. In the next section, this protocol is applied to experimental images such as the one shown in Fig. 2, with a sub-pixel treatment with $N$ = 4.

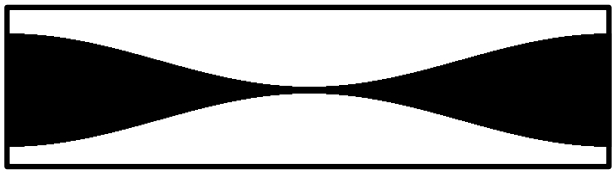

*Figure 3. Synthetic cylinder with sinusoidal perturbation.*

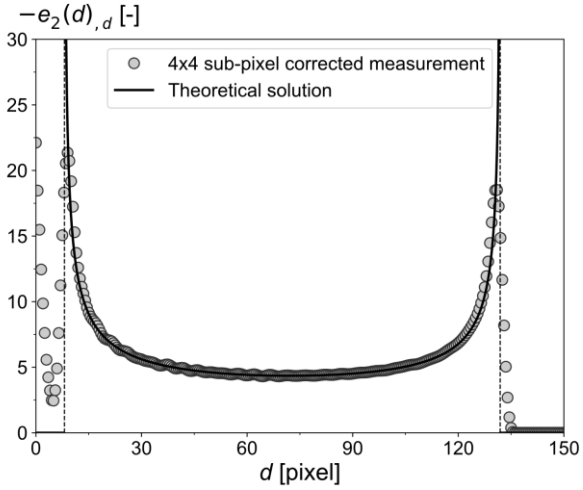


*Figure 4. Derivative of the scale distribution* $-e_2(d)_{,d}$ *of the synthetic object from Fig. 3. Comparison between the theoretical and the measured distribution with a 4x4 sub-pixel treatment.*

## 5. RESULTS

A series of OH* emission and backlighting images are recorded at high-speed frequency with a large field-of-view covering the entire visualization window, such as the one in Fig. 1. Time-averaged images are calculated to visualize the global structure of the subcritical combustion of the propellants. The time-averaged OH* emission

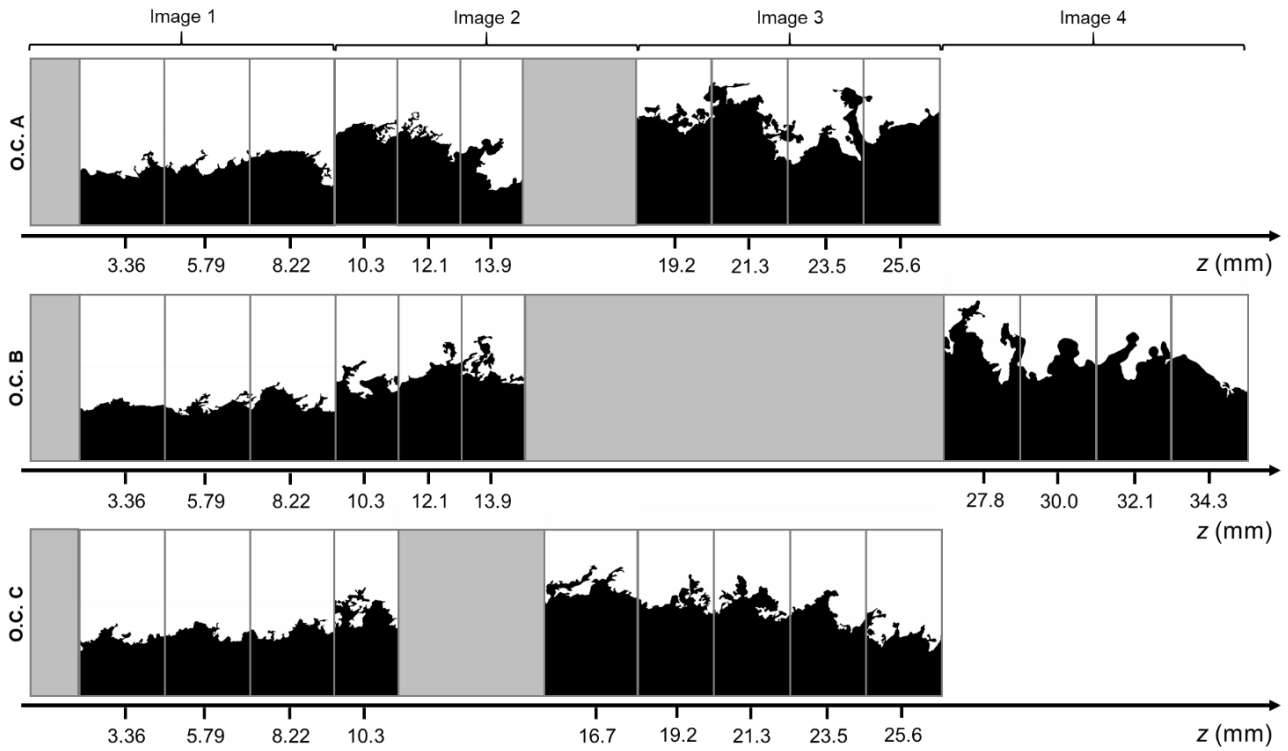


*Figure 6. Snapshots of the segmented liquid-gas interface as a function of the distance z from the injector exit plane. The liquid phase is represented in black, and only the liquid core interface is shown.*

image is then deconvoluted with an Abel transformation to obtain the reaction zone of the flame. The Abel-transformed image is shown in blue in Fig. 5 and is superimposed with the time-averaged backlighting image in grey levels. The resulting composite image is presented in Fig. 5 for O.C. B. This image shows the average relative position between the reaction zone and the atomizing liquid jet. At the near-injector zone, the flame is positioned very close to the liquid jet interface, inside the oxygen/methane mixing layer. At this position, the liquid mist being produced by textural atomization is evaporated and consumed, explaining why so few droplets are seen in that position. Further downstream, the flame spreads radially away from the liquid core. This is likely due to the presence of thicker liquid ligaments at the liquid-gas interface which produce larger drops that will take a longer time to evaporate. This allows the oxygen to move radially away from the liquid core axis before being consumed by the flame. Fig. 5 also shows the positions of the images recorded for the measurements, as indicated in Fig. 1, with white rectangles. The visualized windows represented in Fig. 5 indicate that the observed liquid-gas interface is inside the reactive zone. This jet flame structure, described for O.C. B, is also observed for O.C. A and C.

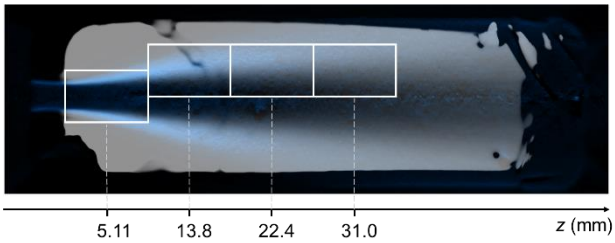


*Figure 5. Superimposition the average backlighting image of the liquid jet (shown in grey levels) and the Abel-transformed image of the OH* chemiluminescence (shown in blue) for O.C. B. White rectangles indicate the image measurement positions 1-4 in relation to the flame structure.*

Fig. 6 shows examples of instantaneous segmented images showing the liquid system in black at the different positions highlighted in Fig. 1. From top to bottom, three horizontal series of instantaneous images are shown with increasing chamber pressure from O.C. A to O.C. C. Certain zones, marked in grey in the figure, could not be analyzed because of the presence of liquid deposits on the visualizing optical window or because of a lack of signal (zone near the injector exit).

The visualized liquid-gas interface shows small-scale deformations which are ligamentous in shape. These deformations constitute the textural atomization process: the ligamentous structures show a series of contracted or swollen regions.

Ligaments of this type have already been reported in other primary atomization studies [5,6] and are likely a result of turbulent fluctuations inside the

liquid phase overcoming the surface tension at the interface. The characteristic size of these turbulent fluctuations increases as the flow moves downstream.

For all three operating conditions represented in Fig. 6, the size, length, number, and shape of the ligaments evolve with the distance $z$ to the injector. Near the injector, ligaments are thin and short. As the distance to the injector increases, ligaments become thicker, longer, and more deformed. Furthermore, most ligaments are oriented streamwise, indicating aerodynamic effects from the coaxial high-speed fuel flow surrounding the liquid jet.

To study the evolution of the textural atomization process with the distance to the injector, and for each operating point, the segmented images are divided into 10 ROIs (9 for O.C. C), each centered at a given distance $z$ from the injector. The width of the ROIs, $w_{ROI,}$ is not constant, varying between 1,74 mm and 2,67 mm. Thus, all results are normalized by $w_{ROI}$ to allow the comparison between ROIs.

Following the methodology established in Section 3, the scale distribution $e_2(d)$ is measured for each snapshot. Fig. 7(a)-(c) report the average scale distribution obtained from 100 images at each ROI for all tested operating conditions. The distributions are shown in the [16 µm, 400 µm] range. The lower limit was evaluated elsewhere [9]. It corresponds to the smallest scale for which the image pixelization does not interfere with the measurements.

As expected, the scale distributions start at a maximum and decrease with the scale $d$. This decrease is the consequence of the reduction of circumference length due to the erosion operation. The reduction in circumference length at scale $d$ represents the circumference length of liquid structures of size equal to or smaller than the scale $d$. As $d$ increases, $e_2(d)$ reaches a constant. The scale at which this asymptote is reached corresponds to the largest scale of the textural ligaments inside the considered ROI.

We see in Fig. 7 that the scale distribution evolves significantly with the distance $z$. Both the height and width of $e_2(d)$ vary. The height of $e_2(d)$ at scale $d$ is representative of the number of liquid structures of that very scale. Thus, for each operating condition, Fig. 7 reports a position $z$ for which the textural ligament structures are most numerous. At this position, the textural atomization process is the most intense. The variation of the width of the distribution $e_2(d)$ with the position bears witness to the evolution in the size of the liquid structures that make up the textural atomization process. Globally speaking, it appears that the ligamentous structures of the textural deformation increase in size with the position $z$. These observations are confirmed by the derivatives $e_2(d)_{,d}$.

The average derivatives $e_2(d)_{,d}$ of the scale distributions at each ROI are plotted, for each O.C., in Fig. 8(a)-(c). As for $e_2(d)$, the distributions are shown in the [16 µm, 400 µm] range. We see that at each position, the distributions report a bell shape. Interpreting this shape is made easy by considering Eq. (1). This equation says that there exists a set of cylinders with a mono-modal diameter distribution that has the same scale distribution as the set of textural liquid structures. It also says that the height of $-e_2(d)_{,d}$ is proportional to the number of cylinders of diameter $d$ (considering that $L_c$ is constant, which we do here). Thus, the textural liquid structures can be seen as a set of cylinders whose population varies as a function of the distance $z$ from the injector. To account for this variation, we introduce the scale $d_p$ at which the mode of the distribution is obtained, the height $H_p$ of this mode ($H_p = -e_2(d_p)_{,d}$) and the half-width at half-maximum $HWHM$ to characterize the dispersion of the size of the liquid structures involved in the textural atomization process.

Fig. 9(a)-(c) plots the values of these three parameters as a function of the distance $z$ and for each O.C. Fig. 9(a) reports a continuous increase of the scale $d_p$ with the position $z$. This denotes a continuous increase of the average size of the liquid structures involved in the textural atomization process. The interesting point shown in Fig. 9(a) is that neither the values of $d_p$ nor its evolution with distance $z$ are influenced by the experimental operating conditions of this work. This observation may be moderated somewhat for O.C. C, for which a constant value of $d_p$ seems to emerge from $z$ = 15 mm. This point would need to be confirmed by further measurements.

Fig. 9(b) reports the height $H_p$ of the distribution as a function of the position and for each O.C. When the distance from the injector increases, $H_p$ increases, reaches a maximum, and then decreases. As indicated above, $H_p$ reports information on the number of structures of a given scale or on the volume of liquid involved in these structures. Then, when $H_p$ increases, the textural structures contain more and more liquid, and when $H_p$ decreases, the textural structures contain less and less liquid. The position at which $H_p$ is maximum is therefore the position at which the textural atomization process is the most intense in terms of the amount of liquid it involves. The interesting point to be noted in Fig. 9(b) is that, as for the scale $d_p$, the parameter $H_p$ reports no significative dependence on the O.C.

Finally, the distribution dispersion represented by the parameter $HWHM$ is shown in Fig. 9(c) as a function of the position $z$ for each O.C. Generally speaking, we see that $HWHM$ increases with the distance $z$ illustrating the fact that the scale range of the textural liquid structures enlarges when the distance from the nozzle increases. As for the two previous parameters, Fig. 9(c) reports no significant effect of the pressure on the scale dispersion of the textural atomization process.

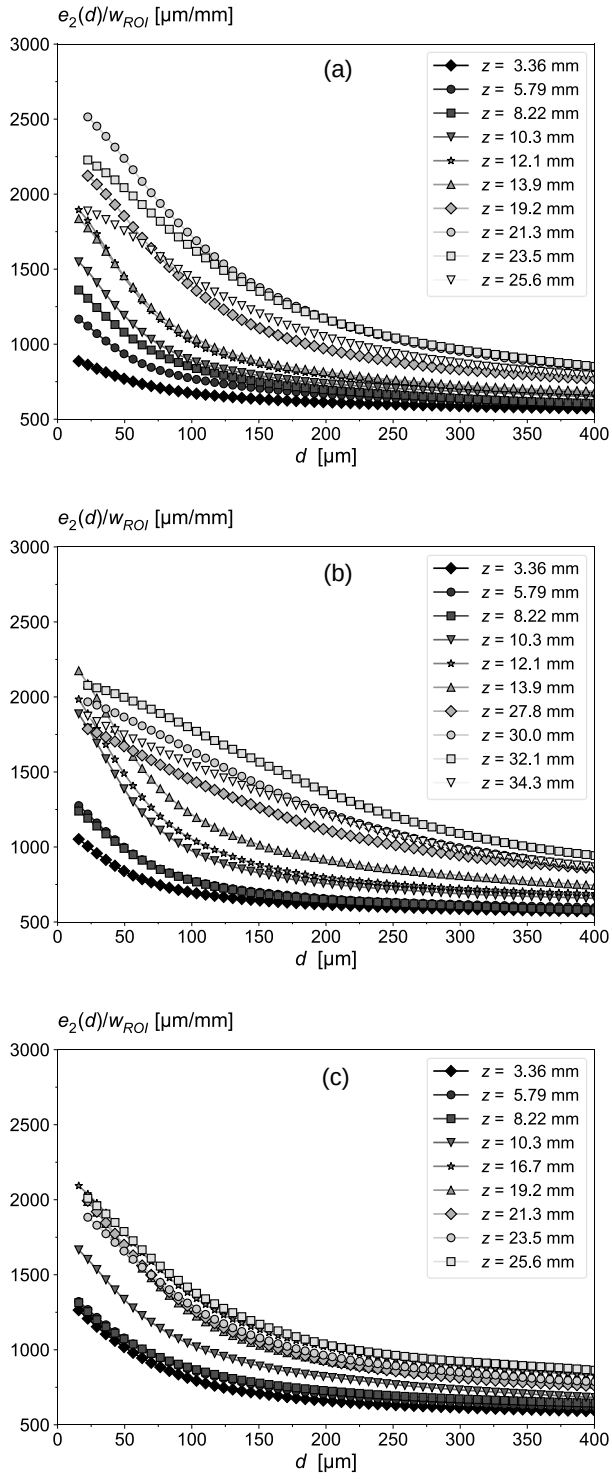


*Figure 7. Average scale distribution $e_2(d)/w_{ROI}$ at each position z for operating condition (a) A, (b) B, and (c) C. One in every third point is shown.*

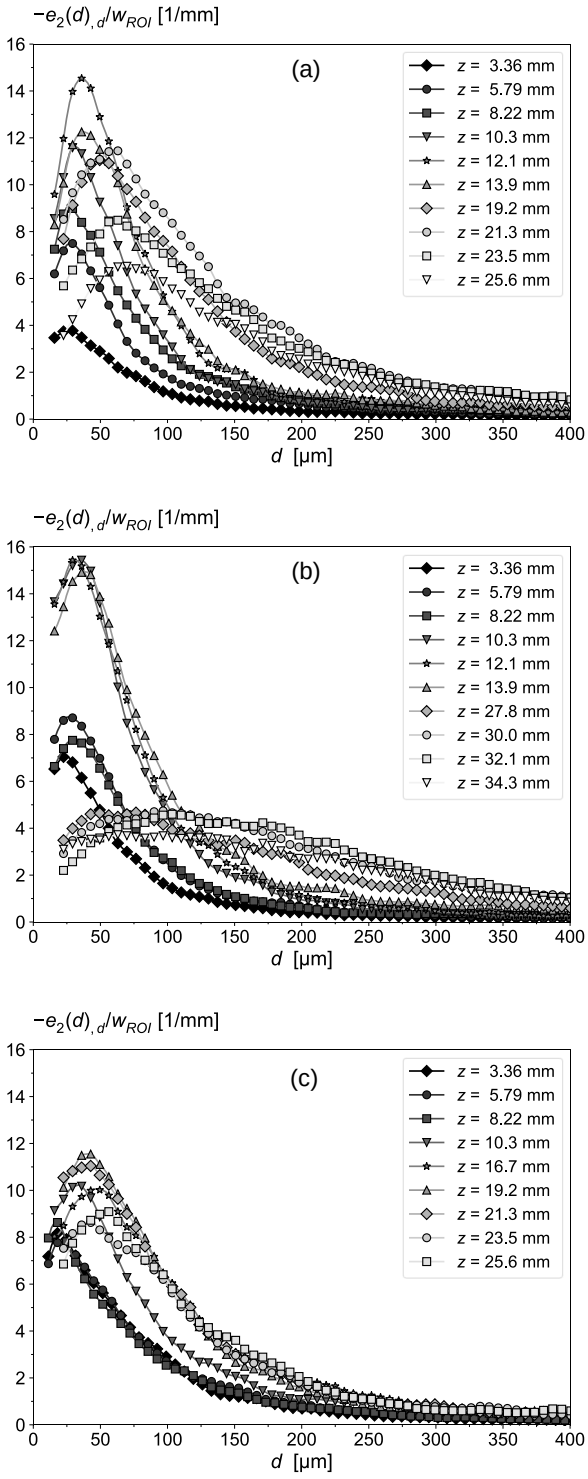


*Figure 8. Average $-e_2(d)_{,d}/w_{ROI}$ distribution at each position z for operating condition (a) A, (b) B, (c) C. One in every third point is shown.*

The not significant influence of the chamber pressure on the textural liquid structures confirm that, in line with the scenario proposed by Wu et al. [6], the production of the textural ligaments is mainly controlled by the turbulence of the liquid flow.

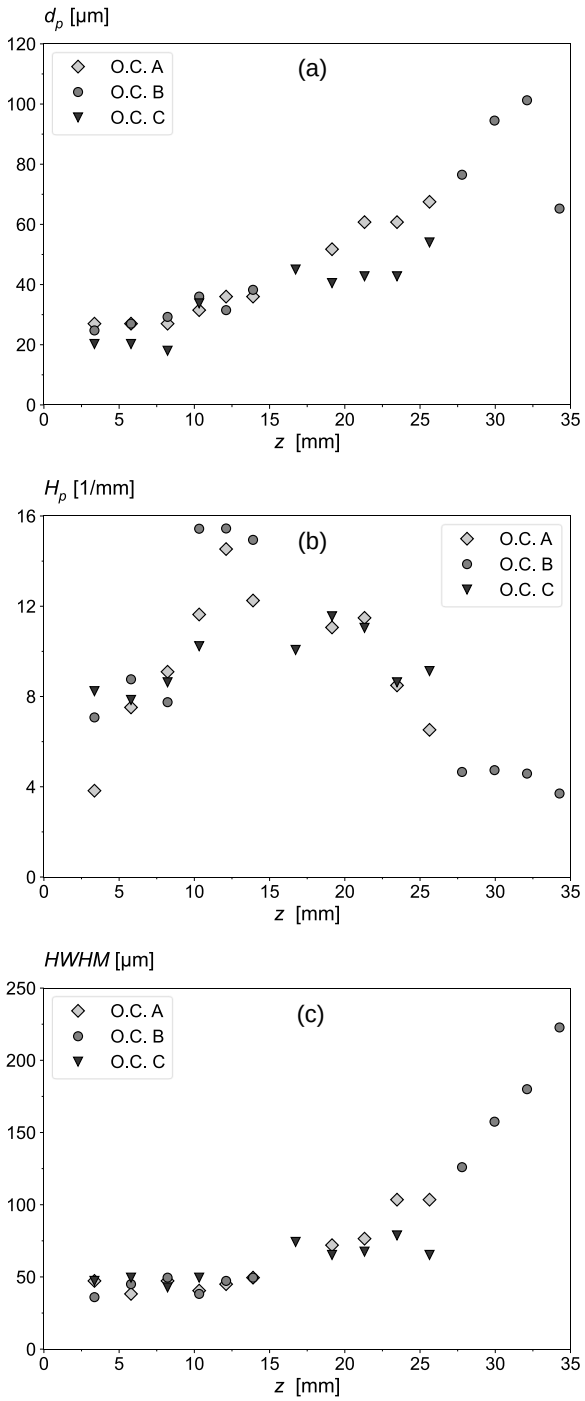


*Figure 9. Evolution with distance z of* $-e_2(d)_{,d}$ *distribution descriptors (a) peak scale* $d_p$*, (b) maximum height* $H_p$*, and (c) half-width at half maximum (*HWHM*). Comparison of the three operating conditions.*

## 6. CONCLUSION

The present work reports measurements of average scale distributions of liquid ligaments attached to the LOx jet as visualized in high-resolution backlighting images under reactive conditions for three subcritical operating conditions. The scale distributions $e_2(d)$ and their derivatives $-e_2(d)_{,d}$ provide valuable information on the textural liquid structures of the primary atomization process. The measured scale distributions show that the textural ligamentous liquid structures can be associated with a set of cylinders whose diameter distribution is mono-modal and that has the same scale distribution as the one measured. One found here that the main characteristics of the diameter distribution (position of the maximum, height of the maximum, and width of the distribution) are not significantly influenced by the chamber pressure. This result says that, for the tested operating conditions, the textural atomization process is controlled by the liquid jet turbulence.

The evolution of the characteristics of the diameter distribution with the distance to the injector exit plane gives information on how the spray produced by the textural atomization process varies in space. Close to the injector, the droplets are small and their diameter disperses very little. Furthermore, the amount of liquid involved in the spray is small. As the distance from the injector increases, the results suggest that the size and dispersion of the drops increase while the amount of liquid involved in the atomization process first increases and then decreases. Thus, the position at which the amount of liquid is maximum is where the textural atomization process is most intense.

The general behavior described in this work can serve as a guide for the development of numerical primary atomization models. In addition, the mathematical estimation of some local drop diameter distributions from the scale distributions could serve as input information for these models where the local size of primary drops is required.

## REFERENCES


[1] Lux J, Haidn O (2009). Flame Stabilization in High-Pressure Liquid Oxygen/Methane Rocket Engine Combustion. Journal of Propulsion and Power, 25,n°1:15-23.

[2] Dumouchel C (2008). On the experimental investigation on primary atomization of liquid streams. Exp. in Fluids, *45*, 371-422.

[3] Lasheras and Hopfinger (2000). Liquid jet instability and atomization in a coaxial gas stream. Ann. Rev. Fluid. Mech. 32:275-310.

[4] Dumouchel C, Blaisot JB, Abuzahra F, Sou A, Godard G, Idlahcen S (2019). Analysis of a Textural Atomization Process. Exp. In Fluids 60:133

[5] Wu PK, Miranda RF, Faeth GM (1995). Effects of initial flow conditions on primary breakup of

nonturbulent and turbulent round liquid jets. Atomization and Sprays, 5:175-196.
[6] Wu PK, Tseng LK, Faeth GM (1992). Primary breakup in gas/liquid mixing layers for turbulent liquids. Atomization and Sprays, 2:295-317.
[7] Hoyt JW, Taylor JJ (1977). Waves on water jets. Journal of fluid mechanics, 83-1:119-127.
[8] Marmottant P, Villermaux E (2004). On spray formation. Journal of fluid mechanics, 498:73-111.
[9] Geiger L, Fdida N, Dumouchel C, Blaisot JB, Dorey LH, Théron M (2024). Multiscale analysis of textural atomization process in a rocket engine coaxial assisted jet, Exp. in Fluids, under revision.
[10] Habiballah M, Orain M, Grisch F, Vingert L, Gicquel P (2006). Experimental studies of high-pressure cryogenic flames on the Mascotte facility. Combustion Science and Technology 178(1-3):101-128.
[11] Fdida N, Vingert L, Ristori A, Le Sant Y (2016). Droplet size and velocity measurements in a cryogenic jet flame of a rocket-type combustor using high-speed imaging. Atomization and Sprays 26(5):411-438.
[12] Boulal S, Fdida N, Matuszewski L, Vingert L, Martin-Benito M (2022). Flame dynamics of a subscale rocket combustor operating with gaseous methane and gaseous, subcritical or transcritical oxygen. Combustion and Flame 242:112179.
[13] Grenard P, Fdida N, Vingert L, Dorey LH, Selle L, Pichillou J (2019). Experimental investigation of heat transfer in a subscale liquid rocket engine. Journal of Propulsion and Power 35(3):544-551.
[14] Vingert L, Fdida N, Mauriot Y, Ortega Colomer I, Irimiea C, Delhaye D, Mohamed AK, Corbas V, Théron M (2019). Experimental Investigations of Liquid Oxygen/Methane Combustion at Very Low Mixture Ratio at the Mascotte Test Facility. 32nd ISTS & 9th NSAT Joint Symposium.
[15] Dumouchel C, Thiesset F, Ménard T (2022). Morphology of contorted fluid structures. Int. Journal of Multiphase Flows 152:104055.
[16] Dumouchel C, Cottier L, Renoult MC (2023). Fine characterization of the capillary instability of free viscoelastic jets. Journ. Non-Newtonian Fluid Mechanics 322:105135.
[17] Phansalkar N, More S, Sabale A, Joshi M (2011). Adaptive local thresholding for detection of nuclei in diversity stained cytology images. 2011 International conference on communications and signal processing 218-220).